

# Radially polarized, half-cycle, attosecond pulses from laser wakefields through coherent synchrotron-like radiation

F. Y. Li<sup>1</sup>, Z. M. Sheng<sup>1,2,\*</sup>, M. Chen<sup>1,†</sup>, L. L. Yu<sup>1</sup>, J. Meyer-ter-Vehn<sup>3</sup>, W. B. Mori<sup>4</sup>, and J. Zhang<sup>1</sup>

<sup>1</sup> Key Laboratory for Laser Plasmas (Ministry of Education) and Department of Physics and Astronomy, Shanghai Jiao Tong University, Shanghai 200240, China

<sup>2</sup> SUPA, Department of Physics, University of Strathclyde, Glasgow G4 0NG, UK

<sup>3</sup> Max-Planck-Institut für Quantenoptik, D-85748 Garching, Germany

<sup>4</sup> University of California, Los Angeles, California 90095-1547, USA

Attosecond bursts of coherent synchrotron-like radiation are found when driving ultrathin relativistic electron disks in a quasi-one-dimensional regime of wakefield acceleration, in which the laser waist is larger than the wake wavelength. The disks of overcritical density shrink radially due to the focusing wake fields, thus providing the transverse currents for the emission of an intense, radially polarized, half-cycle pulse of about 100 attoseconds in duration. The electromagnetic pulse first focuses to a peak intensity 10 times larger ( $7 \times 10^{20} \text{ W/cm}^2$ ) than the driving pulse and then emerges as a conical beam. Basic dynamics of the radiative process are derived analytically and in agreement with particle-in-cell simulation. By making use of gas targets instead of solids to form the ultrathin disks, the new scheme allows for high repetition rates required for applications.

PACS numbers: 52.38.Kd, 52.59.-f, 52.59.Ye, 42.65.Ky

## I. Introduction

Great efforts have recently been devoted to obtain attosecond bursts of coherent extreme-ultraviolet (XUV) and soft x-ray radiations. They open the door to exploring and controlling processes of the microcosm such as attosecond spectroscopy of bound electrons [1]. So far, established methods for producing such pulses are based on high harmonic generation from atomic gases, where the driving laser intensity is limited below  $10^{16} \text{ W/cm}^2$  [2]. High harmonic generation from solid plasma surface [3] makes use of relativistic optics ( $> 10^{18} \text{ W/cm}^2$ ) [4] and allows for much brighter sources. These harmonics correspond to trains of attosecond pulses in the time domain, and can be used to isolate single attosecond spikes using high-pass filters [5]. By temporally rotating either the surface geometry [6] or the driver wavefront [7], individual spikes can be obtained even without filtering. Single attosecond pulses can also be produced from relativistic electron sheets formed by laser interaction with nanometer foils [8] or by nanobunching at solid surfaces [9]. Wu *et al.* considered a double-foil setup irradiated by an ultraintense few-cycle laser pulse and the generation of relativistic electron sheets from the first production foil by direct laser acceleration. Under oblique incidence, laser beam reflection at the second foil provides the transverse current, which emits an intense  $p$ -polarized half-cycle attosecond pulse [10].

In the present paper, we propose a new path, producing single intense attosecond pulses from underdense plasmas rather than solids. By making use of gas plasmas as a target, the condition of ultrahigh laser contrast is greatly relaxed and a bright source allowing for high repetition rate may become possible. It has been known that relativistic plasma waves excited by

an intense short laser pulse exhibit strong accelerating and focusing fields for electrons, and promise acceleration to high energies over a short distance [11]. In most experiments the laser beam is tightly focused to reach highest possible intensity  $I_0$  with waist  $W_0 \leq \sqrt{a_0} \lambda_p / \pi$ , where  $\lambda_p$  is the plasma wavelength and  $a_0 = 8.5 \times 10^{-10} \lambda_0 [\mu\text{m}] \sqrt{I_0 [\text{W/cm}^2]}$  the normalized laser amplitude at wavelength  $\lambda_0$ . Plasma electrons within the laser path is then pushed sideways by strong laser radiation pressure ( $\propto \nabla_r I$ ), creating bubble-like wakes. Some electrons circling around the bubble sheath are transversely injected at the rear vertex [12] and accelerated forming a narrow bunch [13]. This is the concept of bubble wakefield acceleration [14]. An important feature is that the accelerating bunch oscillates in the wake wave forced by the focusing fields and emits bright betatron x-rays [15].

Here, we make use of a different regime of wakefield acceleration, occurring for the driving laser waist larger than the wake wavelength. We refer to it as quasi-one-dimensional (quasi-1D) regime, since wake electrons are now dominated in 1D longitudinal motion, at least for those close to the laser axis. Correspondingly, the density wave crests show disk-like profile as visualized in experiments [16]. Most notably, they converge into dense sheets when driven to high nonlinearities or close to wave breaking. These ultrathin density crests have been used as relativistic flying mirrors for laser backscattering [17]. Attosecond XUV/x-ray pulses can be produced this way due to time compression and frequency upconversion by Doppler shift factors of  $\sim 4\gamma_p^2$ , where  $\gamma_p = (1 - v_p^2/c^2)^{-1/2}$  with  $v_p$  the phase velocity of the plasma wave.

In the present work, we follow another line that does not require a second pulse, but leads to self-emission of an intense attosecond pulse from the dense electron sheet itself. For this to happen, we consider breaking of the above wake-wave symmetries that leads to injection of the ultrathin density crest (or the electron sheet) into the wakefield. As we shall see, the electron sheet contracts in transverse direction right after injection due to radial focusing wake fields, while boosted in energy primarily by longitudinal wakefield acceler-

---

\*zsheng@sjtu.edu.cn  
or zhengming.sheng@strath.ac.uk  
†minchen@sjtu.edu.cn

ation. The central new observation here is that a strong radially polarized, half-cycle, attosecond (RHA) pulse is emitted by the transverse currents established during the initial contraction phase. This coherent attosecond burst of electromagnetic pulses differs in several aspects from the wakefield based betatron x-rays normally obtained so far [15]. It is also found that wakefield acceleration plays a crucial role in amplifying the radiation fields. The radiation reaction damps and eventually saturates the fields, resulting in a high-energy (few mJ) attosecond pulse of relativistic intensity.

The remainder of the paper is organized as follows. Section II discusses how to inject an electron sheet into the wakefield and, in particular, a self-injection scenario based on density transition is briefly summarized. In Sec. III, the generation of RHA pulses from the injected electron sheet is described using particle-in-cell (PIC) simulations. Comparisons with normal betatron radiations obtained from wakefield acceleration are discussed. In Sec. IV, a simplified model is built for illustrating the basic dynamics of RHA generation. In Sec. V, additional effects beyond the simplified model are discussed and verified using PIC simulations. Scaling of the RHA generation with laser parameters is also studied. Finally, section VI summarizes the whole paper and discusses the experimental conditions required.

## II. Electron sheet injection into quasi-1D wakefield

Different ways may, in principle, be used to induce injection of electron sheets into wakefield [18]. A direct and promising approach was recently described using density-gradient injection in a controlled manner. The details of the scheme are documented in Ref. [19], where an up-ramp density profile followed by a plateau is employed. Wave breaking then occurs sharply at the density transition position and leads to a sudden longitudinal injection into the quasi-1D wakefield. This is in contrary to the transverse injection that normally occurs quasi-continuously in the bubble regime [12, 14]. Notice that longitudinal injection but in gentle way has recently been observed in experiments [20]. The key elements of the present sharp longitudinal injection are as follows. First, along the up-ramp, the first few wake wave periods trailing after the driving laser can travel at superluminal speeds. This is valid for high nonlinearities, so that the wake wave crests can be stably compressed into dense sheets without premature injection [19, 21]. The free of injection eventually terminates as the waves propagate into the following plateau density region, where the wave's phase velocity falls below the light speed. As a result, a major part of the sheet electrons satisfying the injection threshold are trapped as whole in a very short time scale. They typically form an ultrathin (10s nanometers thick corresponding to attoseconds in duration) overcritical dense electron disk that accelerates in the wakefield.

## III. Attosecond pulse generation via particle-in-cell simulation

The evolution of an injected electron sheet in the wakefield and the associated radiation flash are first illustrated in

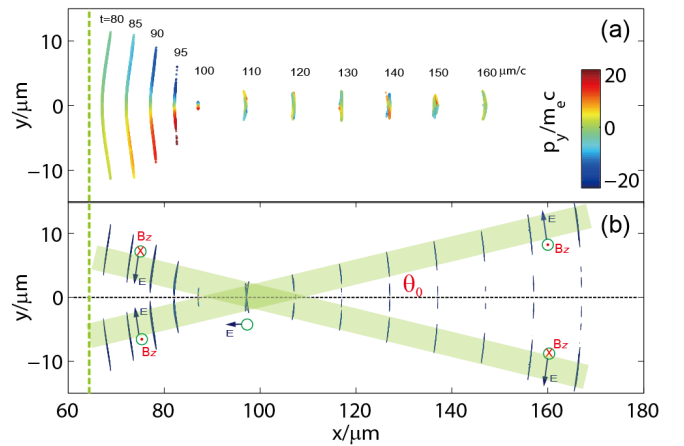


FIG. 1: (Color online). (a) Snapshots of trapped electron sheet at different times (given as label) colored according to transverse momentum  $p_y$  and (b) the radiated attosecond pulses given as contour plot of  $B_z^2$ . The dashed line on the left side marks the position of sharp injection of electron sheet. The full density pattern of the wake is given in Fig. 2(b) for  $t = 160 \mu\text{m}/c$ . These results are obtained from 2D PIC simulation in  $x$ - $y$  plane. In full 3D geometry, the emission appears as an annular beam propagating as a radially polarized, half-cycle, attosecond (RHA) pulse along a cone with opening angle  $\theta_0 \sim 10^\circ$ , indicated as shaded stripes.

Figs. 1(a) and 1(b). It is seen that the sheet contracts in transverse direction to a smallest diameter in tens of laser periods right after the injection, while accelerating longitudinally up to highly relativistic  $\gamma$ -factors (compare Fig. 4). It is in this short time interval that the attosecond pulse is emitted. As found in Fig. 1(b), the pulse is first attached to the electron sheet, but then propagates along a cone, while the electrons move closer to the axis in a channel of almost constant diameter.

These results are obtained from 2D PIC simulations using the code OSIRIS [22]. As a demonstration case, the controlled self-injection scenario [19] is employed to induce injection of electron sheets. The simulation parameters are detailed as follows. A linearly polarized (along  $z$  direction), 18 fs (FWHM of intensity) laser pulse of peak intensity  $I_0 = 7.7 \times 10^{19} \text{ W}/\text{cm}^2$  irradiates an underdense plasma slab with a density ramping-up front of  $65 \mu\text{m}$  long. The plateau density is  $n_0 = 0.04n_c$  with  $n_c = 1.74 \times 10^{21} \text{ cm}^{-3}$  the critical density for laser wavelength  $\lambda_0 = 0.8 \mu\text{m}$ . A laser waist of  $W_0 = 17 \mu\text{m}$  is used and large enough for the formation of wide sheets in quasi-1D regime. An electron temperature of  $T_e = 20 \text{ eV}$  is initialized to mimic field ionization by prepulses. In the simulation, spatial grids of  $\Delta x \times \Delta y = 158 \times 25$  per square micron and time steps of  $\Delta t = 0.00625 \mu\text{m}/c$  are employed and fine enough to resolve the attosecond features; we have checked that even higher resolution gives nearly the same results.

We now analyze the radiative process in general. The injected electrons are diverted by focusing wake fields toward the central axis according to  $d\beta_\perp/dt \simeq \varepsilon_\perp/\gamma$ . Here,  $\beta_\perp$  is the normalized transverse velocity;  $t$  and the focusing field  $\varepsilon_\perp$  have, respectively, been normalized by  $\omega_0^{-1}$  and

$E_0 = m_e \omega_0 c / e$  with electron mass  $m_e$ , elementary charge  $e$  and laser frequency  $\omega_0 = 2\pi c / \lambda_0$ . Near the center axis, the focusing field,  $\varepsilon_\perp \propto n_0 r$ , is almost linear in both radius  $r$  and ambient density  $n_0$ . For the present parameters, the betatron strength parameter [23] of the trapped electrons typically amounts to a few tens. These electrons perform synchrotron-like motion with curvature radius  $\rho \simeq \lambda_0 \gamma / (2\pi \varepsilon_\perp)$  and emit broad-band radiation with cut-off frequency  $\omega_c \simeq 3\gamma^3 c \rho^{-1}$  [24]. There are a couple of new features compared with normal betatron radiation [15]. First, the high density of the electron sheet, typically larger than the critical density  $\sim 10^{21} \text{ cm}^{-3}$  [19], enables synchrotron-like radiation in a coherent manner. Coherency occurs provided that sufficiently large number of electrons reside in a volume of scale length on the order of the radiation wavelength in the rest frame of electrons. For the present case, it is equivalent to

$$n_s \gg 10^{13} \varepsilon_\perp^3 \gamma^4 \text{ cm}^{-3}, \quad (1)$$

where radiation at the cut-off wavelength  $\lambda_c = 2\pi c / \omega_c$  is assumed. Considering that  $\varepsilon_\perp \sim 0.1$ , this criterion can be readily met even for  $\gamma \sim 100$ . As a result, the coherency is well preserved at the initial contraction phase, during which the trapped sheet electrons are only accelerated up moderate energies (less than 50 MeV in the present case). After that the sheet electrons are confined within a small radius and shall emit normal betatron x-rays which are incoherent and orders of magnitude weaker in intensity. Second, due to axial symmetry and inward acceleration of disk electrons, radially polarized half-cycle electromagnetic pulses are produced during contraction. For the present case, due to the ultra-relativistic feature of sheet electrons, the dephasing time (arising from velocity mismatch between radiation and sheet) is much longer than the contraction period (i.e., from injection to focused to axis), which is typically a few tens of laser periods as shown in Fig. 1(a). Therefore, the radiated pulse is almost overlapped with the sheet profile during the contraction phase and naturally has an attosecond duration. It is interesting to mention that radially polarized half-cycle pulses have recently been demonstrated from thin photoconductors, where a sequence of annulus microelectrodes are fabricated on the surface to induce radial currents [25]. However, due to the static wafer plane, only pulses of picosecond duration are generated, determined by the lifetime of the radiating currents.

These features are well illustrated by the sample simulation. Figure 2(a) records how the peak field  $B_z^{max}/B_0$  of the RHA pulse evolves with time, where  $B_0 = m_e \omega_0 / e$  is the normalizing field. According to Fig. 1(b), the attosecond pulse emerges in three stages: field amplification during initial sheet contraction, beam crossing on axis, and finally annular beam propagating along a cone. At the stage of beam crossing, the emission is focused to a maximum of  $B_z^{max}/B_0 \geq 18$ , indicated by the shaded region in Fig. 2(a). This corresponds to a peak intensity greater than  $7 \times 10^{20} \text{ W/cm}^2$ , almost 10 times larger than the driving pulse. After beam crossing on axis (e.g.,  $t > 130 \mu\text{m}/c$ ), the upper and lower branch of the pulse propagate separately in space and the actual peak field shows up as  $B_z^{max}/B_0 = 4.5$ , corresponding to  $4.3 \times 10^{19} \text{ W/cm}^2$  in intensity or  $\sim 2 \times 10^{13} \text{ V/m}$  in field strength. It then slowly

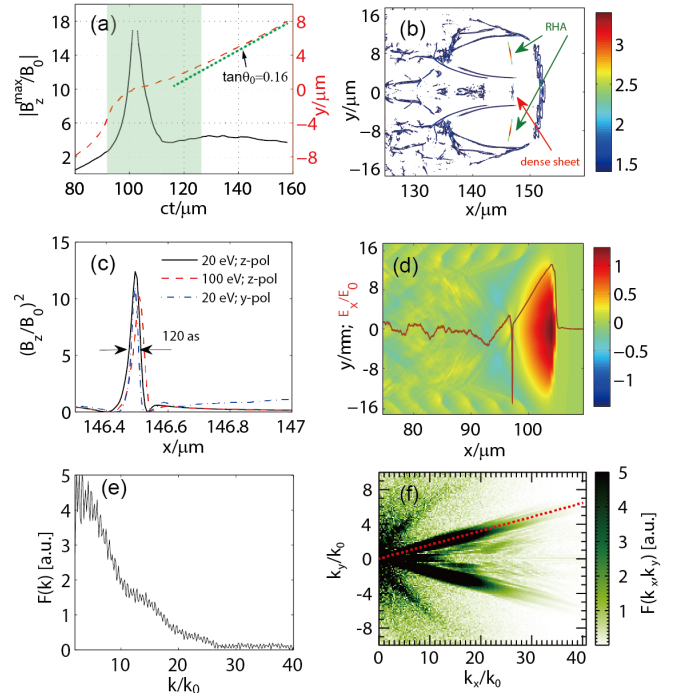


FIG. 2: (Color online). (a) Evolution of peak field  $|B_z^{max}|/B_0$  (solid) and associated  $y$  coordinate (dashed) of the RHA pulse versus time. The shaded region refers to beam crossing stage as explained in the text. The green dotted line indicates the slope of propagation direction. (b) Contour plots of the electron density  $n/n_c$  and  $|B_z/B_0|$  (sharing the same color bar) at  $t = 160 \mu\text{m}/c$ . The wake wave has developed a complex broken-wave pattern, in particular to the sides bordering unperturbed plasma and downstream. The only features relevant to this paper are the tiny dense sheet of relativistic electrons (marked by red arrow) and the RHA pulse (marked by green arrows). (c) Line-outs of  $(B_z/B_0)^2$  along  $y = 8.32 \mu\text{m}$  at  $t = 160 \mu\text{m}/c$  for three cases corresponding to different initial plasma temperatures (20 and 100 eV) and  $y$  or  $z$  polarization of driving laser. (d) Snapshot of longitudinal electric field  $E_x$  at  $t = 110 \mu\text{m}/c$ ; the red curve ( $\times 10$ ) shows on-axis profile. (e) Line-out along one of the branches given in Fig. 2(f) shows a broad-band XUV spectrum extending up to  $k/k_0 \simeq 25$  or about 40 eV in photon energy, where  $k_0 = 2\pi/\lambda_0$ . (f) 2D spatial spectrum of the RHA pulse at  $t = 160 \mu\text{m}/c$  and line-out along the dashed line is given in (e).

decays due to diffraction.

Figure 2(b) shows how the RHA pulse propagate at later time in the wake. It is found that the initial quasi-1D wake is evolving into a complex broken-wave pattern due to laser evolution [26]. The half-cycle pulses as short as 120 as [see Fig. 2(c)] are propagating inside the wake, but deviated from the center axis. The corresponding spatial spectrum of the pulse given in Fig. 2(f) shows clearly two branches, each with a small divergence. The line-out along one of the branches given in Fig. 2(e) shows a broad-band XUV spectrum extending up to  $k/k_0 \simeq 25$  or about 40 eV in photon energy, where  $k_0 = 2\pi/\lambda_0$ . In the present sample simulation, the annular beam (assuming a beam diameter equals to the transverse dimension of the present 2D pulse) carries a total energy of  $\sim 12 \text{ mJ}$ , which is about  $2 \times 10^{-3}$  of the incident laser energy.

The RHA generation is found to be insensitive to finite

thermal temperature. The emission profile hardly changes when increasing  $T_e$  up to 100 eV as depicted in Fig. 2(c). Also shown in this subfigure is the resulting emission profile when switching the polarization direction of the driving pulse from  $z$  to  $y$  (within the simulation plane) axis. Few differences are observed, indicating that the polarity of the attosecond emissions is independent of the driving pulse, but only determined by the transverse contraction motion of sheet electrons. We have confirmed using 3D PIC simulations (not shown here) that the annular attosecond light beam is uniform in intensity azimuthally, corresponding to radial polarization. Notice that full-scale 3D simulations for the present configuration cause extremely heavy computational loads due to the wide box dimensions and high resolutions required for both longitudinal and transverse directions, so that they have to be performed with much lower resolutions compared with the above 2D simulation. However, they confirm very well the half-cycle profile and the radial polarity of the attosecond emissions.

#### IV. Simplified model for attosecond pulse generation

The basic dynamics of RHA generation can be derived using a simplified model. It assumes that a flat, monoenergetic electron sheet of delta-like density profile  $n_s = \delta(x/\sigma_s)$  with finite areal density  $\sigma_s = \int n_s dx$  and no initial transverse momentum is injected into a wakefield of uniform accelerating and focusing fields. Coherent radiation from the electron sheet is then described by the 1D wave equation  $(\partial^2/\partial x^2 - c^{-2}\partial^2/\partial t^2)E_{y,r} = \epsilon_0^{-1}c^{-2}\partial J_{y,r}/\partial t$ , where  $J_{y,r} = -ec\beta_{y,r}n_s$  is the radiating current with  $\beta_{y,r} = \int_{\tau_0}^{\tau_1} d\beta_y \ll 1$  the velocity integrated over a short transverse acceleration [10]. The radiated field  $E_{y,r}$  can be first calculated in the rest frame of the sheet with Lorentz factor  $\sim \gamma$  and then transformed back to the laboratory frame. The result is given by

$$E_{y,r} \simeq \left(\frac{\sigma_s}{\epsilon_0}\right)\beta_{y,r}^R\gamma, \quad (2)$$

where  $\beta_{y,r}^R$  denotes the velocity  $\beta_{y,r}$  in the rest frame. Equation (2) indicates that the radiated power,  $\propto |E_{y,r}|^2 \propto \gamma^2$ , grows with the electron energy. On the other hand, the Lorentz factor  $\gamma$  evolves following from  $d\gamma/dt = -\vec{\beta}_x \cdot \vec{E}_x - \vec{\beta}_y \cdot \vec{E}_y$ . Taking into account the radiated fields  $E_{y,r}$ , the total fields can be expressed as  $\vec{E}_x = \vec{E}_{x,w}$  and  $\vec{E}_y = \vec{E}_{y,w} + \vec{E}_{y,r}$ , where  $\vec{E}_{x,w}$  and  $\vec{E}_{y,w}$  are the longitudinal and transverse wake fields, respectively. Inserting the above field components as well as the expression of Eq. (2), the energy equation reads

$$\frac{d\gamma}{dt} + \frac{\sigma_s}{\epsilon_0}\beta_{y,r}^R\beta_y\gamma - \beta_y E_{y,w} - \beta_x E_{x,w} = 0. \quad (3)$$

Assuming  $\gamma(t=0) = 1$  initially, wakefield acceleration first boosts  $\gamma$ -factor rapidly, which then saturates due to radiation damping at a rate  $(\sigma_s/\epsilon_0)\beta_{y,r}^R\beta_y$ . Saturation occurs for  $\vec{\beta}_x \cdot \vec{E}_x + \vec{\beta}_y \cdot \vec{E}_y = 0$ , which leads to the saturated field

$$E_{y,r}^{sat} \simeq E_{x,w}/\tan\theta + E_{y,w}, \quad (4)$$

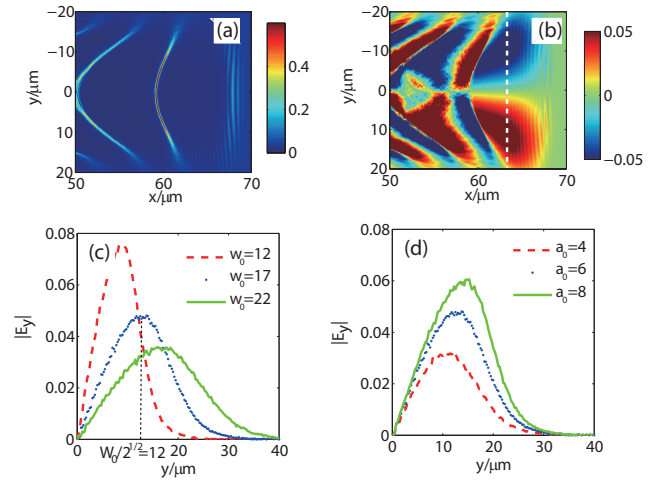


FIG. 3: (Color online). Snapshots of (a) electron density  $n_e/n_c$  and (b) transverse wake field  $E_{y,w}/E_0$  taken when the first wake wave period is approaching the density plateau region. Transverse line-out of  $E_{y,w}$  along  $x = 63 \mu\text{m}$  [see the vertical dashed line in (b)] for (c) different driving laser waists and for (d) different laser amplitudes.

where  $\tan\theta = \beta_y/\beta_x$  is evaluated at the saturation instant. It is clear from the above analysis that wakefield acceleration has played an essential role in RHA generation. At this point, the present case differs from the half-cycle emission from the double-foil setup, where the relativistic electron sheet emerging from the second foil is almost fixed in  $\gamma$  and is supposed to radiate immediately the strongest fields [10]. Equation (4) further suggests that  $E_{y,r}^{sat}$  can be large provided that  $\tan\theta \simeq \beta_y$  is small initially and, in an ideal case, the saturated level can also be maintained for a long period.

#### V. Additional multi-dimensional effects

There are a couple of effects not yet included in the above simplified model which has assumed a flat electron sheet. In the sample simulation, the injected sheet is not perfectly flat but slightly curved as seen in Fig. 1(a). Owing to the sharp longitudinal injection, a curved wake wavefront [16, 17] will directly map into the initial spatial profile of injected sheet. More importantly, the injected electrons will also inherit certain transverse velocities. These will cause transverse contraction during propagation even without the focusing wake fields, and the radiative process is ultimately limited by deformation of the sheet profile.

To see qualitatively the initial transverse velocity distribution and how it scales with laser parameters, we analyze single electron dynamics in the wakefield. To the zeroth-order, the normalized transverse velocity (e.g.,  $\beta_y$ ) changes as  $d\beta_y/dt = (1/\bar{\gamma})(-E_{y,w} + \beta_x B_{z,w})$ , where  $B_{z,w}$  is the static magnetic fields generated in a laser wake [27], and  $\bar{\gamma}$  is the Lorentz factor averaged over laser cycles. The laser ponderomotive force is weak in transverse direction and is not included. In the sample case, the initial velocities of the sheet electrons are equal to that shortly before sharp injection. Consid-

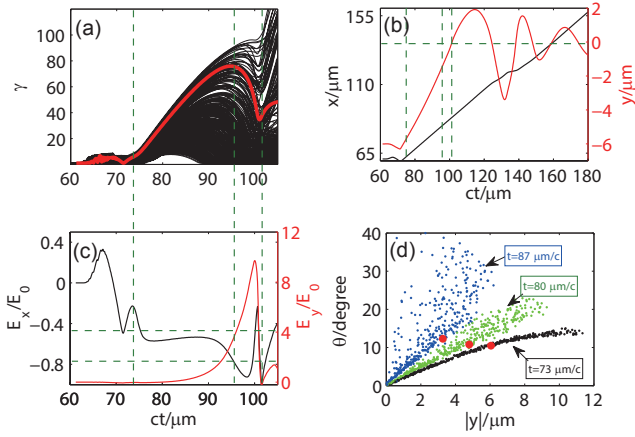


FIG. 4: (Color online). Particle tracking of 400 uniformly distributed electrons picked from the lower half of the sheet at  $t = 80 \mu\text{m}/c$ . (a) Their  $\gamma$  factors versus time. The red curve highlights a typical electron which was initially located near the center of the lower half and belongs to the most energetic ones after acceleration. Time histories are presented for this electron in terms of (b) its coordinates and (c) the electric fields  $E_x$  and  $E_y$  felt by it. The vertical dashed lines (from left to right) marks, respectively, the time of injection,  $\gamma$  saturation and reaching  $y = 0$ . (d) Distributions of the propagation angle  $\theta \simeq (180^\circ/\pi) \arctan \beta_y$  for these electrons versus  $|y|$  at the times indicated;  $t = 73 \mu\text{m}/c$  corresponds to just before injection. The red dots refer to the typical electron defined in (a).

ering a cold start for plasma electrons, i.e.,  $\beta_y(t = -\infty) = 0$ , the transverse velocity at the apex of the first wake wave crest can be given as  $\beta_y = -\int_{-\infty}^t (1/\bar{\gamma}) E_{y,w} dt$ , where contributions from  $B_{z,w}$  are omitted since  $\beta_x$  changes sign during a plasma oscillation. As a consequence, the initial transverse velocities are mainly determined by the transverse wake fields  $E_{y,w}$ , and larger  $E_{y,w}$  generally results in larger  $\beta_y$ .

The electron density of the wake wave approaching the density plateau is plotted in Fig. 3(a) and the corresponding transverse wake fields  $E_{y,w}$  in Fig. 3(b). The transverse line-outs of  $E_{y,w}$  along  $x = 63 \mu\text{m}$  are given in Figs. 3(c) and 3(d) for different laser parameters. It is found that these line-outs share the similar profile with the maximum at  $y = W_0/\sqrt{2}$ . The transverse distribution profile obtained in the highly nonlinear quasi-1D regime is similar to that of a linear wake, i.e.,  $E_{y,w} \propto y \exp(-y^2/W_0^2)$ , assuming that a Gaussian driving laser is used [23]. Following the above qualitative analysis and considering that the radius of the injected electron sheet normally satisfy  $r_s \leq W_0/\sqrt{2}$  [19], the sheet electrons at larger radii have experienced larger  $E_{y,w}$  and thereby take larger initial transverse velocities. As we shall see, this velocity distribution is useful for understanding a couple of simulation results beyond the simplified model.

Below we adopt particle tracking to illustrate these additional effects. A group of electrons picked uniformly from the lower half of the sheet are selected and tracked. As seen in Figs. 4(a-c), the electrons are injected at about  $t = 74 \mu\text{m}/c$  and focus to the axis at about  $t = 102 \mu\text{m}/c$ . During this period, these electrons develop a broad  $\gamma$  spread primarily due to the longitudinal injection dynamics. Figure 5 shows the

trapped sheet during the contraction phase. It is found that the electron sheet could be treated as a sequence of sub-layers, each of which is monochromatic in energy and can be well described by the simplified model shown above. As we have pointed out, the overcritical density and ultrathin feature of the sheet ensure the coherency of the overall attosecond emissions. Figure 4(d) further shows snapshots of the propagation angles  $\theta \simeq (180^\circ/\pi) \arctan \beta_y$  of these electrons at different times, either shortly before injection or during the following contraction phase. It can be seen that the corresponding  $\beta_y$ -values are larger for larger radii (i.e., with larger  $|y|$  coordinates) and they further increase slowly with time due to transverse acceleration. This velocity distribution is in agreement with the above qualitative analysis.

The transverse velocity distribution suggests that the disk-like electron sheet can also be subdivided into a sequence of ring-shaped segments defined by their  $\beta_y$ -values. Applying the simplified model to each ring segment and rotating the coordinate frame by angle  $\theta \simeq \arctan \beta_y$  with respect to the normal  $x$ - $y$  axis, the resulting pointing direction of the radiated electric fields will deviate somewhat from the  $y$  axis; see the schematic drawing in Fig. 1(b). An evidence for this angle deviation is given in Fig. 2(d), where a sharp negative  $E_x$  field shows up at the on-axis overlapping joint during the stage of beam crossing. Moreover, the radiations emitted from segments of different  $\beta_y$  (or  $\theta$ ) will converge due to propagation. This just accounts for the focusing effect observed in Fig. 2(a). The finally observed RHA pulse builds up from all segment contributions weighted according to Eq. (2). As it turns out, largest contributions stem from ring segments with medium radius. For the present case, the conical angle  $\theta_0$  of the radiation peak is measured to be  $\tan \theta_0 \simeq 0.16$  as shown in Fig. 2(a). To evaluate this peak field, a typical electron is highlighted in Fig. 4; it is initially located near the center of the lower half and belongs to the most energetic ones after acceleration. According to Eq. (4), the peak field amounts to  $E_{y,r}^{sat} \simeq E_x / \tan \theta_0 = 4.7$ , where  $E_x \simeq 0.75$ , extracted from Figs. 4(a) and 4(c), is the longitudinal electric field felt by the electron when its Lorentz factor  $\gamma$  becomes saturated, and

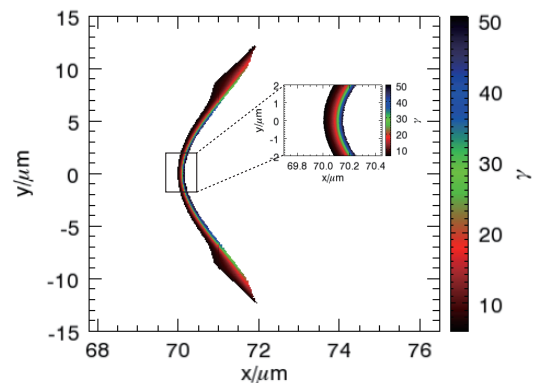


FIG. 5: (Color online). Snapshot of injected electron at  $t = 160 \mu\text{m}/c$  colored according to the  $\gamma$ -factor. The inset shows zoom-in plot of the small rectangle region.

$E_{y,w} \ll E_{x,w}$  is omitted here. This result is in fair agreement with  $B_z^{max}/B_0 = 4.5$  observed after  $t \sim 130 \mu\text{m}/c$ .

We have further checked that the RHA generation is robust against changing laser and plasma parameters. Following Figs. 3(c) and the analysis therein, larger focal spots of driving pulse lead to smaller initial transverse velocities of the injected sheet; therefore, higher radiated field amplitudes are expected according to Eq. (4). This is verified in Fig. 6(a), where  $B_z^{max}$  and  $\theta_0$  scale almost linearly with  $W_0$ . While scanning the laser amplitude  $a_0$  for fixed plasma density  $n_0 = 0.04n_c$ , an optimal value of  $a_0 \sim 6$  for RHA generation (means producing the largest field amplitude) exists as seen in Fig. 6(b). This is because the sheet injection requires high enough driving laser amplitudes [19]; while for too strong drivers, the quasi-1D wake excitation will be violated for fixed laser focal spot. The scaling dependence with the plasma density  $n_0$  becomes even more complicated, because the laser conditions has to be adjusted accordingly to make the sheet injection possible.

## VI. Summary and discussions

In conclusion, we have identified a novel attosecond burst of coherent synchrotron-like radiation from laser wakefield acceleration. The attosecond feature does not derive from solid surface layers [9] or ultrathin solid foils [10], but arises from intrinsic features of nonlinear plasma waves, namely steepening and breaking. It makes use of quasi-1D wake wave breaking, allowing to trap a dense electron sheet into

the wakefield. The electron sheet contracts in transverse direction, while boosted in energy, and is found to emit an intense half-cycle attosecond pulse. Pulse energies over 10 mJ can be obtained with the laser-to-RHA conversion efficiency exceeding  $10^{-3}$ . Besides being a bright source for attosecond applications, this burst will also provide useful diagnostics for wavebreaking dynamics [28] in the highly nonlinear quasi-1D regime and corresponding electron sheet injection [19].

It is worthwhile to emphasize that the coherent half-cycle attosecond pulse emerges at the contraction phase of the electron sheet right after the sharp injection. After completely focused to the axis, these electrons are confined within a smaller radius [see Fig. 1(a) and Fig. 2(b)] due to wake evolution and transport for a long distance with highly relativistic energies. They perform significant betatron oscillations and shall also emit incoherent keV-level x-rays as those normally found with wakefield accelerated electrons [15]. Therefore, in real experiments, the present scheme will deliver both a coherent attosecond XUV pulse laterally and an incoherent x-ray beam in the forward direction. Since the number of trapped electrons in the quasi-1D regime with controlled injection can be made higher (such as nC) [19], it may also provide the possibility for brighter betatron radiation with better control when compared with normal self-injections.

The required experimental conditions for RHA generation are within current technical capabilities. Petawatt lasers, presently coming up, will provide sufficiently high power for the high intensities and relatively broad focal spots preferable here. The sample simulation case shown above used a single 350 TW driving pulse delivering 6.5 J in  $\sim 20$  fs. These parameters are well within the ELI-facility capabilities [29] and are also becoming available commercially. The conical angle of the RHA beam is typically less than  $10^\circ$ , thereby allowing refocusing even at half-meter distance by a concentric mirroring tube with diameter less than 16 cm; such techniques have already been implemented in the measurement of wakefield-based electro-optic shocks [30]. The RHA pulse should also be easily distinguished from other sources due to its radial polarization and hollow pattern.

## Acknowledgment

ZMS would like to thank the OSIRIS Consortium at UCLA and IST (Lisbon, Portugal) for providing access to OSIRIS 2.0 framework. FYL thanks helpful discussions with Prof. H.-C. Wu. This work is supported in part by the National Basic Research Program of China (Grant No. 2013CBA01504), the National Natural Science Foundation of China (Grant No. 11121504, 11374210 and 11374209), and the MOST international collaboration project (Grant No. 2014DFG02330). Simulations were supported by Shanghai Supercomputer Center and by the center for high performance computing at SJTU.

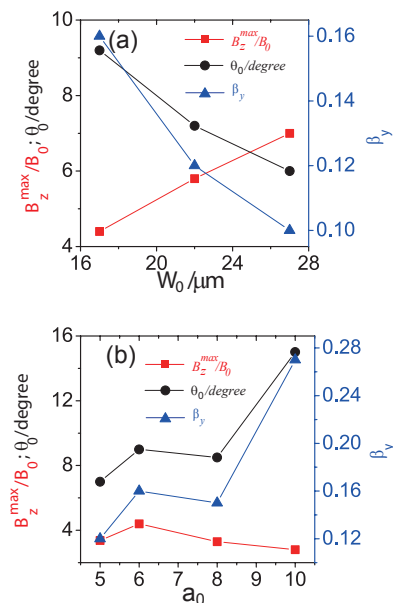


FIG. 6: (Color online). Peak radiation field  $B_z^{max}$  (solid square),  $\theta_0$  defined in Fig. 1 (solid circle), and  $\beta_y$  for the ring segment (as explained in the text) emitting the peak field (solid triangle) versus (a) laser waist  $W_0$  while keeping  $a_0 = 6$  and  $n_0 = 0.04n_c$  fixed, and versus (b) driver amplitude  $a_0$  while keeping  $W_0 = 17\mu\text{m}$  and  $n_0 = 0.04n_c$  fixed.

- [1] F. Krausz and M. Ivanov, *Rev. Mod. Phys.* **81**, 163 (2009).
- [2] P. B. Corkum and F. Krausz, *Nat. Phys.* **3**, 381 (2007); K. Midorikawa, *Jap. J. Appl. Phys.* **50**, 090001 (2011).
- [3] U. Teubner and P. Gibbon, *Rev. Mod. Phys.* **81**, 445 (2009).
- [4] G. A. Mourou, T. Tajima, and S. V. Bulanov, *Rev. Mod. Phys.* **78**, 309 (2006); G. Mourou and T. Tajima, *Science* **331**, 41 (2011).
- [5] A. Pukhov, T. Baeva, D. an der Brügge, and S. Münster, *Eur. Phys. J. D* **55**, 407 (2009); G. D. Tsakiris, K. Eidmann, J. Meyer-ter-Vehn, and F. Krausz, *New J. Phys.* **8**, 19 (2006).
- [6] N. M. Naumova, J. A. Nees, I. V. Sokolov, B. Hou, and G. A. Mourou, *Phys. Rev. Lett.* **92**, 063902 (2004).
- [7] J. A. Wheeler, A. Borot, S. Monchocé, H. Vincenti, A. Ricci, A. Malvache, R. Lopez-Martens and F. Quéré, *Nat. Photon.* **6**, 829 (2012); K. T. Kim, C. Zhang, T. Ruchon, J. Hergott, T. Auguste, D. M. Villeneuve, P. B. Corkum, and F. Quéré, *Nat. Photonics* **7**, 651 (2013).
- [8] V. V. Kulagin, V. A. Cherepenin, M. S. Hur, and H. Suk, *Phys. Rev. Lett.* **99**, 124801 (2007); H. C. Wu, J. Meyer-ter-Vehn, J. Fernández, and B. M. Hegelich, *Phys. Rev. Lett.* **104**, 234801 (2010).
- [9] D. an der Brügge and A. Pukhov, *Phys. Plasmas* **17**, 033110 (2010); B. Dromey, S. Rykovanov, M. Yeung, R. Hörlein, D. Jung, D. C. Gautier, T. Dzelzainis, D. Kiefer, S. Palaniyppan, R. Shah, J. Schreiber, H. Ruhl, J. C. Fernandez, C. L. S. Lewis, M. Zepf, and B. M. Hegelich, *Nat. Physics* **8**, 804 (2012); M. Yeung, B. Dromey, S. Cousens, T. Dzelzainis, D. Kiefer, J. Schreiber, J. H. Bin, W. Ma, C. Kreuzer, J. Meyer-ter-Vehn, M. J. V. Streeter, P. S. Foster, S. Rykovanov, and M. Zepf, *Phys. Rev. Lett.* **112**, 123902 (2014).
- [10] H. C. Wu and J. Meyer-ter-Vehn, *Nat. Photon.* **6**, 304 (2012).
- [11] T. Tajima and J. M. Dawson, *Phys. Rev. Lett.* **43**, 267 (1979); E. Esarey, C. Schroeder, and W. Leemans, *Rev. Mod. Phys.* **81**, 1229 (2009).
- [12] I. Kostyukov, E. Nerush, A. Pukhov, and V. Seredov, *Phys. Rev. Lett.* **103**, 175003 (2009).
- [13] G. R. Plateau, C. G. R. Geddes, D. B. Thorn, M. Chen, C. Benedetti, E. Esarey, A. J. Gonsalves, N. H. Matlis, K. Nakamura, C. B. Schroeder, S. Shiraishi, T. Sokollik, J. van Tilborg, Cs. Toth, S. Trotsenko, T. S. Kim, M. Battaglia, Th. Stöhlker, and W. P. Leemans, *Phys. Rev. Lett.* **109**, 064802 (2012).
- [14] A. Pukhov and J. Meyer-ter-Vehn, *Appl. Phys. B* **74**, 355 (2002); W. Lu, C. Huang, M. Zhou, W. B. Mori and T. Katsouleas, *Phys. Rev. Lett.* **96**, 165002 (2006).
- [15] A. Rousse, K. T. Phuoc, R. Shah, A. Pukhov, E. Lefebvre, V. Malka, S. Kiselev, F. Burgy, J. P. Rousseau, D. Umstadter, and D. Hulin, *Phys. Rev. Lett.* **93**, 135005 (2004); S. Corde, K. Ta Phuoc, G. Lambert, R. Fitour, V. Malka, and A. Rousse, *Rev. Mod. Phys.* **85**, 1 (2013).
- [16] N. H. Matlis, S. Reed, S. S. Bulanov, V. Chvykov, G. Kalintchenko, T. Matsuoka, P. Rousseau, V. Yanovsky, A. Maksimchuk, S. Kalmykov, G. Shvets and M. C. Downer, *Nat. Phys.* **2**, 749 (2006).
- [17] S. V. Bulanov, T. Esirkepov and T. Tajima, *Phys. Rev. Lett.* **91**, 085001 (2003); M. Kando, Y. Fukuda, A. S. Pirozhkov, J. Ma, I. Daito, L. M. Chen, T. Z. Esirkepov, K. Ogura, T. Homma, Y. Hayashi, H. Kotaki, A. Sagisaka, M. Mori, J. K. Koga, H. Daido, S. V. Bulanov, T. Kimura, Y. Kato and T. Tajima, *Phys. Rev. Lett.* **99**, 135001 (2007).
- [18] An electron sheet may be externally injected into a broad wake wave driven by petawatt lasers. Possible sheet production methods were proposed, for example, in Refs. [8]
- [19] F. Y. Li, Z. M. Sheng, Y. Liu, J. Meyer-ter-Vehn, W. B. Mori, W. Lu and J. Zhang, *Phys. Rev. Lett.* **110**, 135002 (2013).
- [20] S. Corde, C. Thaury, A. Lifschitz, G. Lambert, K. Ta Phuoc, X. Davoine, R. Lehe, D. Douillet, A. Rousse and V. Malka, *Nat. Commun.* 4:1501 doi: 10.1038/ncomms2528 (2013).
- [21] J. Mu, F. Y. Li, M. Zeng, M. Chen, Z. M. Sheng and J. Zhang, *Appl. Phys. Lett.* **103**, 261114 (2013).
- [22] R. Fonseca *et al.*, *Lecture Notes in Computer Science*. **2331**, 342-351 (Springer Berlin, Heidelberg, 2002).
- [23] E. Esarey, B. A. Shadwick, P. Catravas, and W. P. Leemans, *Phys. Rev. E*. **65**, 056505 (2002).
- [24] T. Shiozawa, *Classical Relativistic Electrodynamics*, Springer-Verlag (Berlin, Heidelberg, 2004), pp77-82.
- [25] K. Kan, J. Yang, A. Ogata, S. Sakakihara, T. Kondoh, K. Norizawa, I. Nozawa, T. Toigawa, Y. Yoshida, H. Kitahara, K. Takano, M. Hangyo, R. Kuroda and H. Toyokawa, *Appl. Phys. Lett.* **102**, 221118 (2013).
- [26] J. Xu, B. Shen, X. Zhang, M. Wen, L. Ji, W. Wang, Y. Yu and K. Nakajima, *New J. Phys.* **12**, 023037 (2010).
- [27] Z. M. Sheng, J. Meyer-ter-Vehn, and A. Pukhov, *Phys. Plasmas* **5**, 3764 (1998).
- [28] A. G. R. Thomas, S. P. D. Mangles, Z. Najmudin, M. C. Kaluza, C. D. Murphy, and K. Krushelnick, *Phys. Rev. Lett.* **98**, 054802 (2007).
- [29] *ELI-Extreme Light Infrastructure Science and Technology with Ultra-Intense Lasers WHITEBOOK*, edited by G. A. Mourou, G. Korn, W. Sandner, and J. L. Collier (THOSS Media GmbH, Berlin, 2011).
- [30] M. H. Helle, D. Kaganovich, D. F. Gordon, and A. Ting, *Phys. Rev. Lett.* **105**, 105001 (2010).